JGR Atmospheres

RESEARCH ARTICLE
10.1029/2024JD042825

Stable Boundary Layers in an Arctic Fjord-Valley System: Evaluation of Temperature Profiles Observed From Fiber-Optic Distributed Sensing and Comparison to Numerical Weather Prediction Systems at Different Resolutions

Laura Mack[1], Marvin Kähnert[2], Quentin Rauschenbach[3], Lukas Frank[4], Franziska H. Hasenburg[5], Jannis-Michael Huss[6], Marius O. Jonassen[4], Megan Malpas[7], Yurii Batrak[2], Teresa Remes[2], Norbert Pirk[1], and Christoph K. Thomas[6,8]

[1]Department of Geosciences, University of Oslo, Oslo, Norway, [2]Development Centre for Weather Forecasting, Norwegian Meteorological Institute, Oslo, Norway, [3]Institute of Oceanography, Universität Hamburg, Hamburg, Germany, [4]Department of Arctic Geophysics, The University Center in Svalbard, Longyearbyen, Norway, [5]Institute of Physics, Johannes Gutenberg University of Mainz, Mainz, Germany, [6]Micrometeorology Group, University of Bayreuth, Bayreuth, Germany, [7]British Antarctic Survey, Cambridge, UK, [8]Bayreuth Center of Ecology and Environmental Research (BayCEER), University of Bayreuth, Bayreuth, Germany

Key Points:

- The temperature structure of stable boundary layers (SBLs) is observed using airborne fiber-optic distributed sensing (FODS) in Adventdalen, Svalbard
- Strong surface-based inversions, fronts and elevated valley inversions are observed, which are characterized by high temperature variance
- The sub-kilometer-scale model represents cold pool and low-level jets (LLJ) well and outperforms the kilometer-scale model, which shows a distinct warm bias

Correspondence to:
L. Mack,
laura.mack@geo.uio.no

Citation:
Mack, L., Kähnert, M., Rauschenbach, Q., Frank, L., Hasenburg, F. H., Huss, J.-M., et al. (2025). Stable boundary layers in an Arctic fjord-valley system: Evaluation of temperature profiles observed from fiber-optic distributed sensing and comparison to numerical weather prediction systems at different resolutions. *Journal of Geophysical Research: Atmospheres*, *130*, e2024JD042825. https://doi.org/10.1029/2024JD042825

Received 28 OCT 2024
Accepted 26 DEC 2024

Abstract Stable boundary layers (SBLs) commonly form during the Arctic polar night, but their correct representation poses a major challenge for numerical weather prediction (NWP) systems. To enable detailed model verification, we performed measurements of the lower atmospheric boundary layer with airborne fiber-optic distributed sensing (FODS), a tethered sonde and ground-based eddy-covariance (EC) measurements during contrasting synoptic forcings in a fjord-valley system in Svalbard. The FODS-derived temperature variances and static stability profiles are used to investigate the spatial and temporal evolution of different inversion types. The strong gradients of the inversions are accompanied by an increased temperature variance, which is related to enhanced buoyancy fluctuations. The observed vertical temperature and wind speed profiles are compared to two configurations of the HARMONIE-AROME system with different horizontal resolutions at 2.5 and 0.5 km. The higher-resolution model captures cold pool and low level jet formation during weak synoptic forcing, resulting in a well-represented vertical temperature profile, while the coarser model exhibits a warm bias in near-surface temperatures of up to 8 K due to underestimated inversion strength. During changing background flow, the higher-resolution model is more sensitive to misrepresented fjord-scale wind directions and performs less well. The results indicate the importance of the ratio between nominal horizontal model resolution and valley width to represent SBL features. Our results underline the substantial benefit of spatially resolving FODS measurements for model verification studies as well as the importance of model and topography resolution for accurate representation of SBLs in complex terrain.

Plain Language Summary Stable boundary layers characterized by increasing enthalpy with height commonly form during the Arctic polar night. Their correct representation remains a major challenge for NWP systems. A recently introduced measurement method to sample air temperature at high spatio-temporal resolution is FODS. Balloon-borne FODS measurements combined with ground-based EC measurements were performed during contrasting weather situations in a fjord-valley system in Svalbard to validate the NWP predictions against the observations. The vertical profiles of temperature and wind speed are compared to two different configurations of the NWP system HARMONIE-AROME, a kilometer-scale version with 2.5 km horizontal resolution and a hectometric-scale version with 0.5 km horizontal resolution. The hectometric-scale model represents common features of SBLs, such as cold pools and low-level jets, well. The kilometer-scale version does not represent these typical SBL features and exhibits a strong warm bias. The study underlines a substantial benefit of FODS measurements for model verification studies and points out the important role of model and topography resolution in NWP systems.

1. Introduction

Long-lived SBLs commonly form in the Arctic during the polar night and represent a crucial state in the land-atmosphere system affecting the near-surface temperature profile. Strong surface-based temperature inversions

are favorable for the persistence of snow, glaciers, and permafrost (e.g., Smith & Bonnaventure, 2017), but at the same time reduce the surface longwave heat loss (Bintanja et al., 2011), representing a possible contribution to Arctic amplification (Taylor et al., 2022).

Despite their prevalence, the accurate representation of SBLs still poses a major challenge in numerical weather prediction (NWP) models (Sandu et al., 2013; J. Day et al., 2024). Numerical weather prediction models exhibit usually either a warm bias (e.g., Tjernstroem et al., 2021) or a cold bias (e.g., Beljaars et al., 2011) in near-surface temperatures, depending on model resolution and model physics. A warm bias typically occurs when turbulent mixing is overestimated (Tjernstroem et al., 2021) resulting in a too deep and thermally inertial boundary layer (Esau et al., 2018). A cold bias usually occurs when turbulence breaks completely down under very stable stratification, leading to a decoupling of atmosphere and surface (Derbyshire, 1999). This results in a self-amplifying cooling process commonly referred to as "run-away" cooling (Beljaars et al., 2011), where turbulence cannot counteract radiative cooling leading to an increase in static stability and further enhancement of surface cooling (e.g., Zilitinkevich et al., 2008). Under these decoupled conditions, very strong surface-based temperature inversions form (e.g., Atlaskin & Vihma, 2012). However, the resulting strong gradients can cause numerical instability and the reduced mixing in SBLs detrimentally influences the model's ability to represent large-scale dynamics correctly (Beljaars & Viterbo, 1998; Sandu et al., 2013). Therefore, a common remedy is to use turbulence parameterizations which intentionally enhance mixing by utilizing long-tail stability correction functions (Cuxart et al., 2006). This in turn leads to the underestimation of inversion strengths and a warm bias in near-surface temperatures (Atlaskin & Vihma, 2012; Beljaars et al., 2011), which usually increases with lower temperatures (Pietroni et al., 2014).

The spatial structure of SBLs is further complicated by the interaction with orography and the underlying surface (Lehner & Rotach, 2018; Serafin et al., 2018). Valley systems feature the development of valley and slope winds, katabatic flows and cold air drainage due to differential cooling along the slopes. In valley bottoms, cold-air pools can form leading to especially strong surface-based temperature inversions with sharp gradients in the form of strong wind speeds aloft, referred to as low-level jet (LLJ) (Banta, 2008). LLJs advect heat and momentum along slopes, such that turbulence is non-locally driven and fetch-dependent (Serafin et al., 2018). The ability to represent these distinct SBL phenomena in NWP models depends strongly on the resolution and representation of topography (Wagner et al., 2014). The interaction of flows with orography and surface heterogeneity triggers the formation of different types of waves including gravity waves, wake flows, and meandering, referred collectively to as submeso-scale motions (Mahrt, 2014). These features are commonly not resolved in current NWP models, but strongly influence turbulent transport by causing wave drag (e.g., Steeneveld et al., 2009), intermittency, and asymmetry in the efficiency of momentum and scalar fluxes (e.g., Li & Bou-Zeid, 2011).

Furthermore, the SBL representation in models is very sensitive to surface characteristics as weakly and very stable regimes can co-occur on small spatial scales (Kähnert et al., 2022). As a result the snow heat flux and its representation in NWP models is a crucial factor (Arduini et al., 2019; Savijärvi, 2014), such that multi-layer snow schemes are utilized for reducing the aforementioned warm bias in NWP model simulations (J. J. Day et al., 2020). All of the above-mentioned SBL processes are critical for forming and correctly representing near-surface inversions in simulations, the evaluation of which is at the heart of this study.

Current operational regional NWP models are typically kilometer-scale (e.g., Müller, Batrak, et al., 2017; Müller, Homleid, et al., 2017), which leads to an improved representation of complex terrain, such as mountainous and coastal regions due to better prescribed topography compared to coarser global NWP models (Køltzow et al., 2019). Increasing the resolution further is a tempting approach to further improve the representation of local valley systems and boundary layer structure. The Norwegian Meteorological Institute runs operationally the AROME-Arctic model at 2.5 km horizontal resolution covering the European Arctic (Müller, Batrak, et al., 2017) and is currently developing an experimental sub-kilometer scale model configuration with a horizontal resolution of 500 m and an increased vertical resolution covering the Svalbard archipelago (Valkonen et al., 2020). As the vertical temperature profile results from the combined effect of the different topographic and meteorological forcing mechanisms, it lends itself particularly well as validation metric for assessing model performance and the impact of model resolution.

To this end, we aim at comparing the vertical temperature profile across the SBL of these two model configurations against observational data. For a proper comparison, the observations need to be continuous in space across hundreds of meters and fine enough in time to capture the evolution of the thermal SBL structure, which

Figure 1. (a) Model domains of the two HARMONIE-AROME numerical simulations (AA25 and AS05) discussed in the present study. Note, that the domain of AS05 was changed compared to the previous study Valkonen et al. (2020). (b) Adventdalen and Adventfjorden (https://toposvalbard.npolar.no/, Norwegian Polar Institute). (c) Measurement setup (not to scale) for the tethered balloon carrying the fiber-optic cable and station location (red circle) with three-dimensional topography (https://toposvalbard.npolar.no/, Norwegian Polar Institute).

calls for an innovative observational technique. We chose airborne fiber-optic distributed sensing (FODS) utilizing a fiber-optic cable suspended from a tethered balloon (Flying Fiber-Optic eXperiment, FlyFOX, Fritz et al., 2021) to measure air temperature profiles at submeter-scale resolution in an Arctic fjord-valley-system during polar night. Fiber-optic distributed sensing is a recently established in situ-measurement method (Thomas et al., 2012), capable of minimally invasive sampling with high temporal (10 s) and spatial (25 cm) resolution over larger distances (here up to 900 m). In this regard, it offers substantial advantages over common vertically resolved temperature measurements from, for example, eddy-covariance (EC) towers (Mazzola et al., 2016), UAV (unmanned aerial vehicles, Mayer et al., 2012), MWR (microwave radiometers, Pietroni et al., 2014) and RASS (radio acoustic sounding systems, Viana et al., 2012). The high spatio-temporal resolution of FODS makes it possible to study fine-grained SBL features, such as submeso-scale thermal fronts, without assuming Taylor's hypothesis of space-time equivalence (e.g., Pfister et al., 2021a, 2021b; Zeeman et al., 2015). Our FODS measurements were aided by a tethered sonde in combination with ground-based EC measurements. The study site is Adventdalen in Svalbard, which represents together with the adjacent fjord (Adventfjorden) a typical Arctic fjord-valley system. Since both FODS and EC studies are still rarely performed under challenging high Arctic conditions (e.g., Mayer et al., 2012; Mazzola et al., 2016; Pirk et al., 2017; Zeller et al., 2021), our measurements provide a unique opportunity for model verification in this Arctic fjord-valley system and is the first study using FODS for detailed NWP verification.

2. Data and Methods

2.1. Site Description and Experimental Setup

The measurements were carried out in a fjord-valley system in Svalbard called Adventfjorden-Adventdalen (Figure 1b). Adventfjorden is an 8 km long side fjord of Isfjorden, the largest fjord on the west coast of Svalbard, and transitions into the valley Adventdalen, a U-shaped southeast-northwest oriented valley of approximately 4 km width which narrows along its 30 km length. It is surrounded by 600–900 m high mountains in the north and 400–500 m high mountains in the south with several narrower side valleys. The measurement location is at the old aurora station (78.20251°N, 15.82903°E), about 3.5 km from the shore of Adventfjorden, which was only marginally covered by sea ice during the measurement period. Two flights with a tethered balloon, carrying a 1977 m long duplexed fiber-optic cable (details in Sec. 2.2), a tethered sonde (DigiCORA TT12, Vaisala) and a reference temperature sensor (iMet-XQ2, InterMet) were performed on 28.01.2024 (18:38–22:05 UTC, maximum height 877 m) and 01.02.2024 (16:51–20:25 UTC, maximum height 823 m) during polar night (Figure 1c). In addition, data from a standard weather station (with wind measurements at 9 m and temperature measurements at 2.1 m) and an EC system (IRGASON, Campbell Scientific) at 2 m height are used. The raw 20 Hz EC data are processed by applying the standard corrections (e.g., Foken, 2017), double rotation and averaging over 1 min to capture only the turbulent motions in the predominantly stably stratified surface layer.

2.2. Fiber-Optic Distributed Sensing (FODS)

Fiber-optic distributed sensing was used for measuring air temperatures at a high spatial (25 cm) and temporal (10 s) resolution (Selker et al., 2006; Thomas et al., 2012) with a precision of ≤0.3 K and a bias of ≈0.03 K (Zeller et al., 2021). This technique has been successfully applied to investigate various boundary layer phenomena including submeso-scale thermal fronts (Pfister et al., 2021b), morning transitions in valleys (Fritz et al., 2021), and cold air layer development (Zeeman et al., 2015).

The FODS instrument (XT-DTS 5 km variant, Silixa Ltd) sends out a laser pulse through a multi-mode fiber-optic cable with 50 μm diameter. The majority of photons are scattered at glass impurities undergoing elastic (Rayleigh) scattering, but a small portion is scattered inelastically (Raman). The Raman scatter contains red-shifted (Stokes shift) photons, the intensity of which is nearly temperature-independent, and blue-shifted (Anti-Stokes shift) photons, the intensity of which exponentially depends on the temperature of the scattering medium. Thus, the ratio of the intensities of red- to blue-shifted Raman scatter (I_{red}/I_{blue}) is exponentially proportional to the temperature. Assuming that the fiber-optic cable is in thermal equilibrium with the surrounding air at each 25 cm segment and does not suffer from radiative artifacts (Sigmund et al., 2017), a dry fiber-optic cable sampled by FODS measures the dry-bulb air temperature. The full post-field calibration is performed using the Python package "pyfocs" (Lapo & Freundorfer, 2020) which applies the mathematical procedures described in des Tombe et al. (2020) for the general calibration equation of

$$T(x,t) = \frac{\gamma}{\ln\left(\frac{I_{red}(x,t)}{I_{blue}(x,t)}\right) + C(t) - \int_0^x \Delta\alpha(x')\,dx'}, \tag{1}$$

where γ is a constant, $\Delta\alpha(x)$ an attenuation correction function, and $C(t)$ a calibration function, that is derived from simultaneously performed reference temperature measurements (Pt1000) in a warm and cold reference bath (Thomas et al., 2012). The length along the fiber is converted to physical heights above surface ground using a linear approximation taking the position and height of the balloon into account. This approximation has been shown to be sufficient compared to non-linear height corrections (Fritz et al., 2021).

The FODS-measured dry-bulb temperature T is converted to potential temperature $\theta = T(p_0/p)^{R/c_p}$ (based on surface pressure p_0, the pressure p as linear fit based on measured pressure at the height of the balloon, the gas constant R, and the heat capacity c_p). The corresponding vertical gradient $\partial\theta/\partial z$ is approximated with a 1 m rolling block average (Fritz et al., 2021). The high temporal resolution also enables to study vertical profiles of temperature variance $\overline{T'^2}$ and potential temperature variance $\overline{\theta'^2}$, describing buoyancy fluctuations, which are related to turbulent potential energy (e.g., Zilitinkevich et al., 2008).

2.3. HARMONIE-AROME

We use model output from two different configurations of the limited-area convection-permitting NWP system HARMONIE-AROME (Bengtsson et al., 2017). The first model data set (AA25) stems from the operational model AROME-Arctic (Müller, Batrak, et al. (2017), operated by the Norwegian Meteorological Institute), which covers a substantial part of the European Arctic (see Figure 1a). AROME-Arctic uses a model grid with 2.5 km horizontal resolution, 65 vertical terrain-following hybrid sigma levels extending up to a height of about 37 km (the lowest at approximately 12 m, 36 m, and 60 m) and a model time step of 75 s in the atmospheric model. The lateral boundary conditions as well as sea surface temperature and sea ice concentration fields are given by ECMWF's IFS-HRES (hourly, with 9 km horizontal resolution). The data assimilation system of AROME-Arctic uses the 3D-Var analysis procedure for initializing atmospheric model variables and optimal interpolation for surface analysis. A 3-hourly assimilation cycle is utilized. The atmospheric model is coupled to the surface model SURFEX (Masson et al., 2013), which describes surface evolution and surface-atmosphere interactions as a one-dimensional vertical process. SURFEX represents processes over four main surface types (natural and urban landscapes, inland water bodies, and seas) and uses a mosaic approach where each model grid cell can contain some fraction of all four principal surface types. Turbulence within the surface layer is parameterized using a first-order closure based on local stability according to Louis (1979). Turbulent diffusion in the atmosphere is parameterized in the vertical using a prognostic 1.5-order TKE-closure with a diagnostic length scale formulation that combines local and non-local stability according to Lenderink and Holtslag (2004).

In an additional modeling experiment (AS05, Valkonen et al., 2020), an updated version of HARMONIE-AROME is run with an increased horizontal resolution of 0.5 km, 90 vertical levels extending up to a height of about 35 km (lowest at approximately 5 m, 15 m, and 29 m), and a model time step of 15 s. This additional numerical simulation was performed for a selected model domain covering the Svalbard archipelago (see Figure 1a).

Compared to AA25, AS05 uses manually corrected land cover data to mitigate the issues found in the original data set (ECOCLIMAP-SG; https://opensource.umr-cnrm.fr/projects/ecoclimap-sg/wiki) applied in AA25. AS05 uses higher resolution land-cover maps than AA25 (30 vs. 300 m nominal resolution) to allow for higher quality of grid-cell-aggregated parameters. Model topography data in AA25 and AS05 are also taken from different sources. AA25 uses the GMTED2010 data (Danielson & Gesch, 2011) set with the nominal resolution of 250 m while AS05 utilizes the ArcticDEM data (Porter et al., 2018) with the nominal resolution of 32 m, refined with Svalbard DTM 5 data (https://inspire-geoportal.ec.europa.eu/srv/api/records/010bfb4a-65aa-4d30-aba9-7d090a432df7) where available. AS05 does not apply data assimilation procedures neither for the atmospheric nor for the surface model variables. To compensate for the lack of observational constraints, AS05 uses more advanced (compared to AA25) multi-layer soil and snow schemes with explicit ground heat flux calculation and multi-energy-budget (Decharme et al., 2011). For the upper air variables, AS05 applies the so-called large-scale mixing approach which allows correcting the state of the model atmosphere based on the host-model data without affecting the high-resolution signal. Similarly to AA25, AS05 uses IFS-HRES as the host model; however, it does not apply the offline ice state correction based on external sea ice drift data utilized in the operational system AROME-Arctic.

Since AS05 unlike AA25 is an experimental system, it does not run on a daily basis. Therefore, when performing the model simulation, the initial state of the model atmosphere was taken from AA25 on 22 January 2024 03 UTC. Thereafter, a short 2-day spin-up period was used to allow for adaptation of the interpolated model state. In the following analysis, we use model fields from the first 24 hr of the respective 00 UTC runs (main cycle) with hourly temporal resolution for both AA25 and AS05.

3. Results

3.1. Evaluation of the Observations

In the following, we briefly describe and interpret the observations for the two performed tethered balloon flights under contrasting meteorological conditions (weak synoptic forcing and change in background flow) during the polar night.

3.1.1. Flight 1 (28.01.2024): Weak Synoptic Forcing

During flight 1 (Figure 2), the FODS-derived potential temperatures span a range of 15 K and the 2 m-temperatures lie below −12°C with a minimum below −15°C.

From the beginning of the flight, a strong surface-based inversion is present characterized by a strong vertical potential temperature gradient (Figure 3a) of more than 0.2 K m^{-1}. The strong temperature gradients co-occur with high temperature variance (Figure 3b). This finding suggests that the vertical potential temperature gradient drives temperature variance, linked to the potential energy of displaced particles from their equilibrium (Zilitinkevich et al., 2008). The surface-based inversion is attached to the ground until it detaches and lifts around 19:10 UTC, which is related to a rapid temperature and wind speed increase (Figures 2b and 2c). Subsequently, as long as the inversion is not attached to the ground, the magnitudes of sensible heat flux and TKE decrease (Figure 2d). Then, at around 19:40 UTC, the near-surface temperature drops by about 2.5 K in less than 5 min, which initiates the formation of a new and deepening surface-based inversion. This process goes along with a decrease in sensible heat flux from about 0 to −30 Wm^{-2}, but an increase in TKE (Figure 2d). The latter can be explained by the increased vertical wind shear in response to the formation of the inversion which counteracts the buoyancy term in the TKE tendency equation (Wyngaard & Coté, 1971). The surface-based inversion again lifts off at 20:00 UTC accompanied by another increase in the near-surface temperature.

In addition to the surface inversions, there are also several elevated weaker inversions present at approximately 450 m, 600 m, and 750 m above ground. These heights correspond to the heights of the surrounding mountains and can therefore very likely be described as valley inversions caused by the advection of the air masses from the

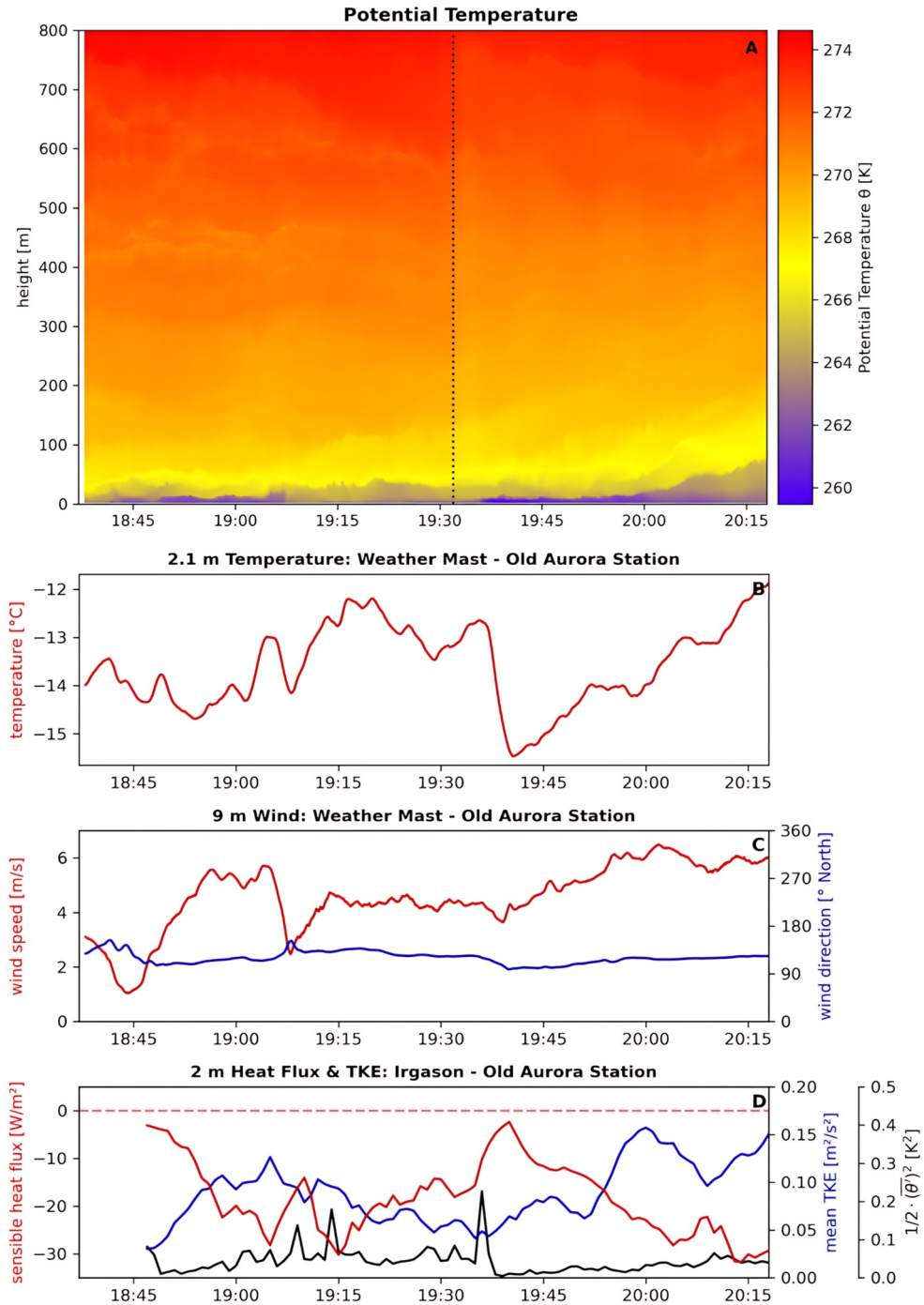

Figure 2. (a) Potential temperature derived from fiber-optic distributed sensing for flight 1. (b) Temperature measured by weather station (2.1 m, red). (c) Wind speed (red) and wind direction (blue) from weather station (9 m). (d) Sensible heat flux (red), TKE (blue), and potential temperature variance (black) derived from the eddy-covariance measurements (2 m) in Adventdalen on 28.01.2024. The vertical, dotted line in panel (a) marks the time when the cold calibration bath was stirred to resolve an unintended stratification. The results are shown for the first part of the flight, when the balloon stayed at an almost constant altitude.

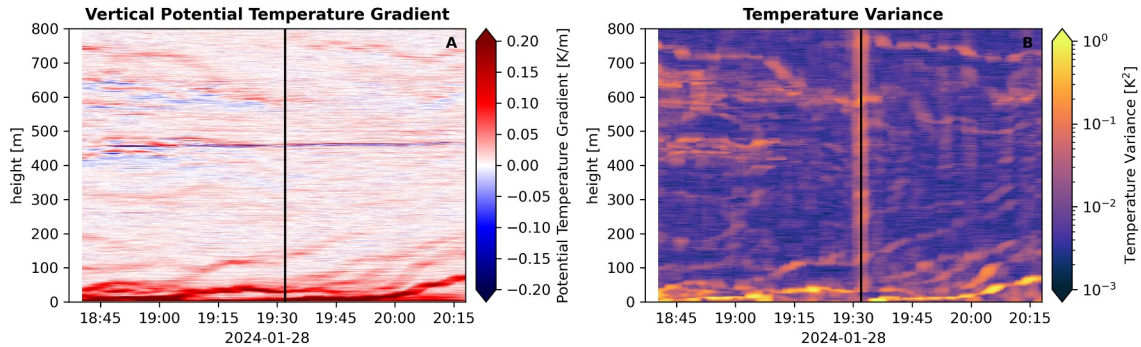

Figure 3. (a) Vertical potential temperature gradient and (b) temperature variance derived from fiber-optic distributed sensing (FODS) (with 5 min temporal average and 1 m spatial average) for flight 1 in Adventdalen on 28.01.2024. The vertical line in both panels marks the time when the FODS cold bath was stirred to resolve an unintended stratification.

mountain plateaus. These valley inversions lie above a layer with unstable stratification (blue color in Figure 3), which indicates that the advected air mass is colder, likely caused by radiative cooling at the mountain plateaus. The valley inversion itself corresponds to the advected surface inversion from the mountain plateaus.

3.1.2. Flight 2 (01.02.2024): Change in Background Flow

The range of potential temperatures for flight 2 was smaller compared to the first flight spanning about 7 K only (Figure 4). The near-surface temperatures lie below −12°C and a strong inversion can be identified from the vertical potential temperature gradient (Figure 5), below which the sensible heat flux is slightly positive (directed upward, Figure 4d). The height of this surface inversion varies on timescales of minutes between 30 and 80 m. The temperature recorded at the weather station decreases when the inversion descends. Above this first inversion, a second elevated inversion is present at around 200 m. The vertical distance between these two inversions remains almost constant. Above this second inversion, the atmosphere is only weakly stratified.

At 18:30 UTC, the potential temperature starts to increase from above and the original surface inversion disappears, while the height of the elevated inversion decreases and attaches to the ground at 19:20 UTC. When the warm air reaches the ground, it manifests itself as a warm front. The warm air advection leads to a decrease in the balloon height to about 500 m around 18:30 UTC by reducing its buoyant lift, but recovers at the end of the warm air advection to about 650 m. A line can be interpolated from the initial sinking trajectory of the balloon to the time at which the warm air reaches the ground (as indicated by the dashed line in Figure 4a) with a height-time tilt of approximately 9 m per minute. The warm front is accompanied by high temperature variance (Figure 5b), indicating enhanced mixing at the interface between the two air layers.

In the weather station observations, three distinct abrupt increases in temperature of about 0.6 K are present (at about 19:15, 19:35, and 20:00 UTC, indicated by the gray shading in Figures 4b–4d), which are accompanied by relatively weak winds. The first pronounced temperature increase (19:15 UTC) co-occurs with a sudden change in wind direction from valley outflow (east/southeast) to inflow (west) conditions from the fjord. When combined with the vertical FODS observations, this abrupt change can be attributed to warm air advection from the fjord, which manifests itself as the tilted warm front with subsequently higher temperatures at higher altitudes. However, the two air flows, that is, cold air outflow versus warm air inflow, compete periodically, until the cold-air layer intensifies again starting from 20:00 UTC, which results in the renewed rise of the balloon and persisting valley outflow at the weather station. During the outflow-inflow transition, extended areas of high temperature variance form from the ground up to a height of 150 m.

3.2. Comparison to Numerical Weather Prediction Systems

This section compares the observations from the two flights with the structure of the modeled Arctic boundary layer for the two different model configurations. We focus here on the surface layer inversion structure and the changes due to the different forcings.

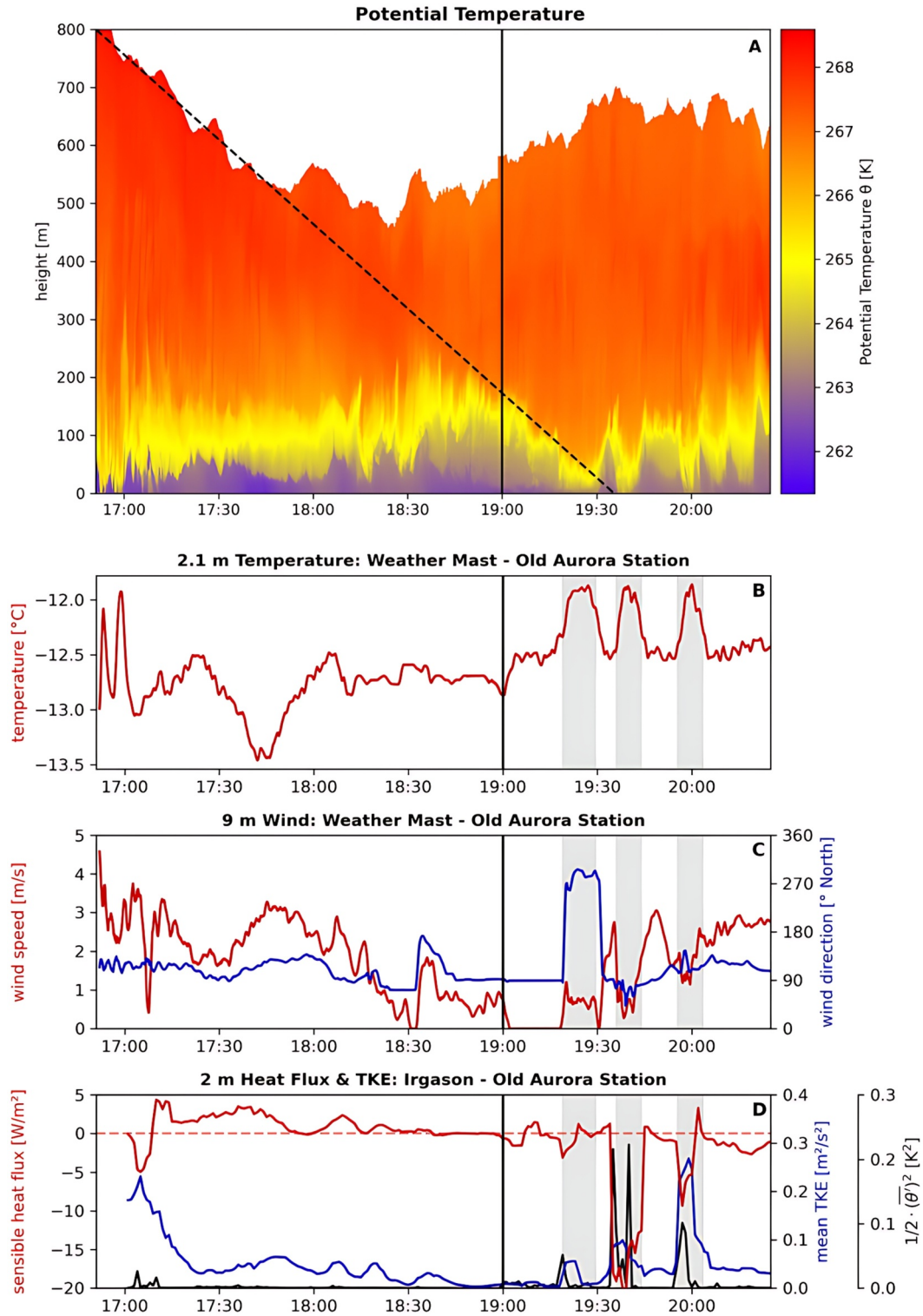

Figure 4. (a) Potential temperature derived from fiber-optic distributed sensing for flight 2. (b) Temperature measured by weather station (2.1 m, red). (c) Wind speed (red) and wind direction (blue) from weather station (9 m). (d) Sensible heat flux (red), TKE (blue), and potential temperature variance (black) derived from the eddy-covariance measurements (2 m) in Adventdalen on 01.02.2024. The dashed line represents the air mass boundary interpolated from the sinking trajectory of the balloon and the vertical line represents imaginary the passage of the warm front at ground level.

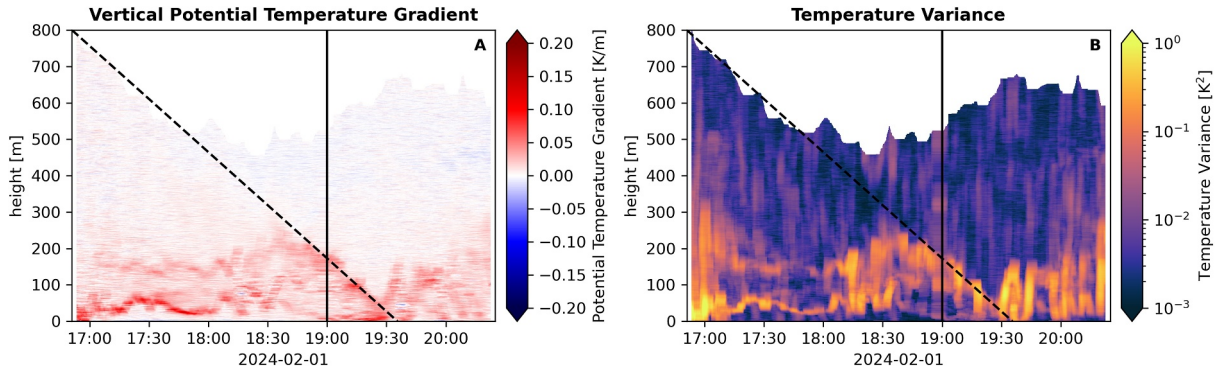

Figure 5. (a) Vertical potential temperature gradient and (b) temperature variance derived from fiber-optic distributed sensing (with 5 min temporal average and 1 m spatial average) for flight 2 in Adventdalen on 01.02.2024.

3.2.1. Flight 1 (28.01.2024): Weak Synoptic Forcing

Figure 6 shows the horizontal temperature distribution at the lowest model level for the Isfjorden area in AA25 (12 m) and the Adventdalen area in AS05 (5 m) with the corresponding land-sea mask. The air over the open water surfaces is relatively warm in both models at around −4°C compared to the elevated mountain areas at about −8°C. In AS05, a pronounced cold pool forms in Adventdalen with temperatures below −14°C that extends to the coast of Adventfjorden. However, the smaller side valleys do not show any cold pool development, which excludes cold-air drainage as formation mechanism and leaves longwave cooling in a combination with sheltering from the large-scale flow resulting in reduced vertical turbulent mixing as reason for its formation. The cold pool starts to form at 17 UTC and intensifies in the following hours (not shown).

Figures 7a and 7b show the vertical profiles of (potential) temperature from AA25, AS05 (closest model grid point), and FODS (averaged over the corresponding hour, i.e., 19–20 UTC). In the averaged FODS observations (black), a strong surface-based inversion is present, extending up to around 150 m, followed by a weakly stable outer layer with several weak valley inversions (Sec. 3.1.1). AS05 (blue) reproduces the shape of the profile and the near-surface temperatures well. The surface inversion in AS05 is stronger than in the observations, which indicates a decoupling of the lowest model levels from the layers above–a process mentioned in the introduction. The inversion in AS05 deepens vertically during night, but the surface temperature remains fairly constant

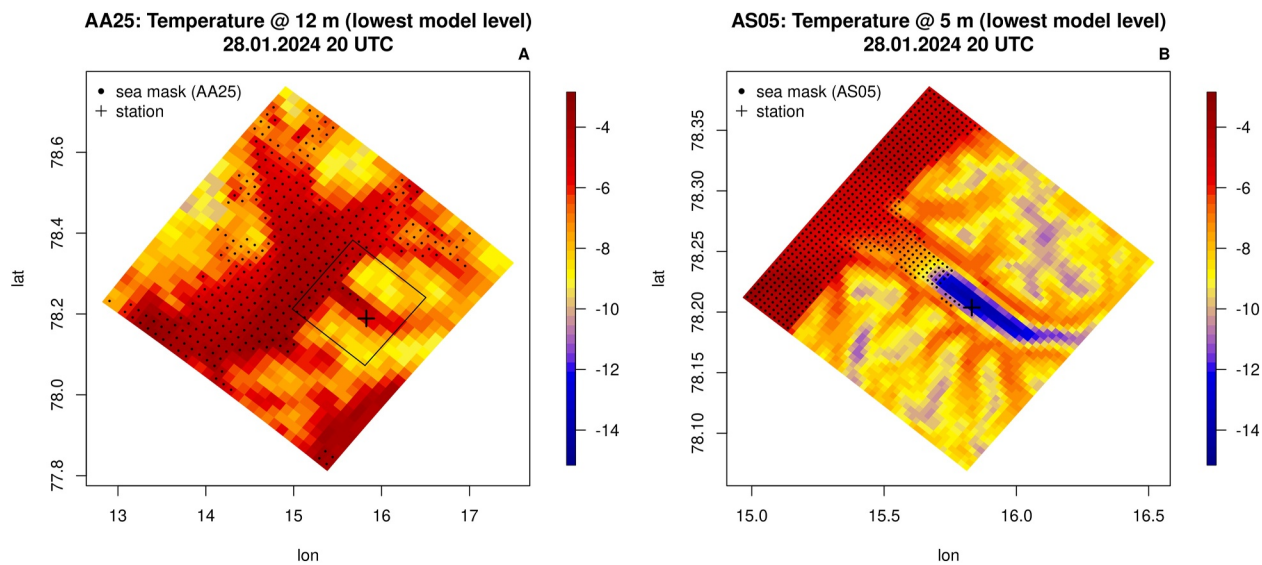

Figure 6. Horizontal temperature distribution [°C] at the lowest model level on 28.01.2024 20 UTC for (a) AA25 (12 m, Isfjorden area) and (b) AS05 (5 m, Adventdalen area, corresponding to the black square) with respective land-sea mask (sea and lake grid points as dots). The black cross represents the Adventdalen station location where the observations were obtained.

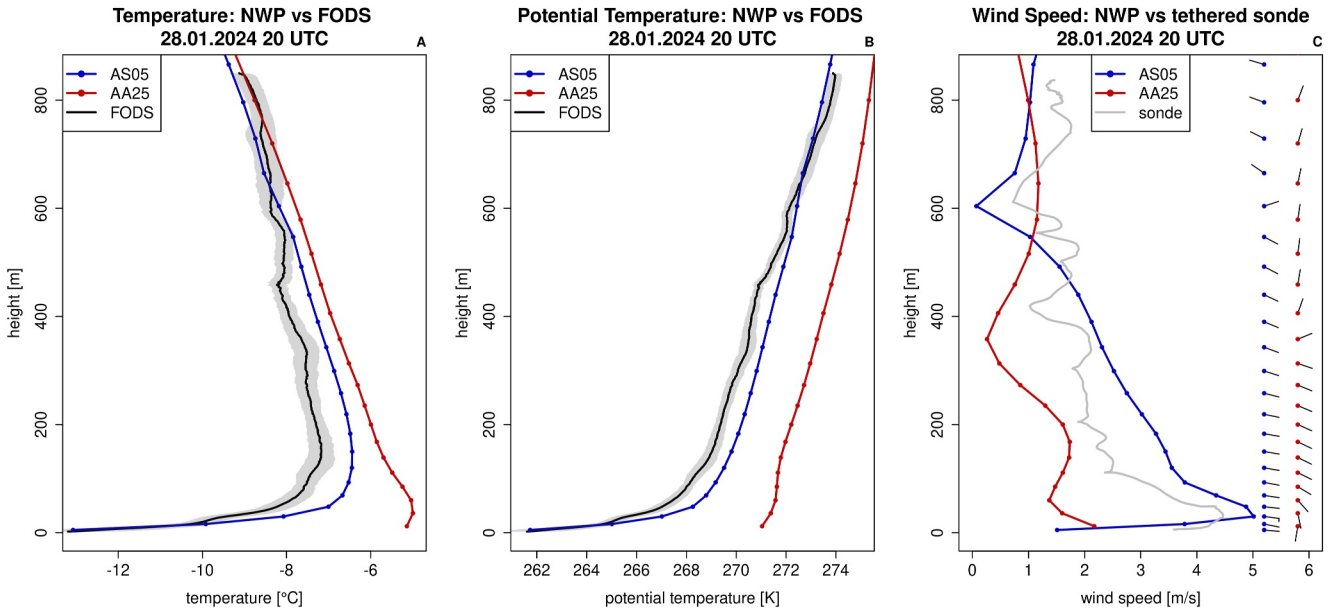

Figure 7. (a) Vertical profiles of temperature from fiber-optic distributed sensing (black, with standard deviation shaded), AS05 (blue), and AA25 (red) on 28.01.2024 20 UTC. (b) Same as (a) for potential temperature. (c) Vertical profiles of wind speed for tethered sonde (gray, during ascend), AS05 (blue), and AA25 (red) with windbarbs.

indicating the absence of run-away cooling. The coarser experiment AA25 (red) does not reproduce the vertical structure of the surface inversion as it does not model the cold-air dynamics, resulting in a strong warm bias of the near-surface temperatures of about 8 K. During the night, the inversion intensifies only slightly reaching a minimum temperature of −6°C at the lowest model level retaining the strong warm bias. The stability of the weakly stable upper layer is reproduced but with an offset of 2 K in potential temperature.

Figure 7c shows the vertical wind profiles. Note that the tethered sonde wind speed profile was measured during the ascent of the balloon (from 17:08 to 17:52 UTC), while the shown model wind profiles are from 20 UTC in accordance with the FODS measurements (Figures 7a and 7b). The measured wind profile shows a LLJ with a maximum wind speed of 4.5 ms^{-1} at 31 m that marks the top of the cold pool. During the descent (21:40 to 22:04 UTC), the LLJ intensified with a maximum wind speed of 7 ms^{-1} at 39 m (not shown). AS05 models a LLJ with maximum wind speed of 5 ms^{-1} at 30 m (i.e., lying in the range of the tethered sonde observations), which also intensifies during night. The wind speed above the LLJ decreases more slowly with height compared to the tethered sonde observations, but both reach a minimum wind speed at 600 m (corresponding to the height of the surrounding mountains), above which the wind direction changes abruptly from outflow to inflow. This vertical profile could be indicative of a land-sea breeze circulation with the LLJ outflow representing the lower branch and the inflow the upper branch, accompanied by air rising over the sea and sinking in the valley. The coarser AA25 does not show a distinct LLJ, but indicates a weak-wind maximum of ~2.2 ms^{-1} at the lowest model level. The wind direction turns with height evenly counter-clockwise from south over east (valley outflow) to north.

3.2.2. Flight 2 (01.02.2024): Change in Background Flow

Figure 8 shows the horizontal temperature distribution in the first hour of the flight of AA25 and AS05 at the respective lowest model level. In both models, the near-surface air temperature over the sea is higher than over the mountain plateaus, although both are higher in AS05 compared to AA25. In both simulations, the warmer air penetrates into the valleys and side valleys.

Figure 9 shows the vertical profiles of observations and models. The FODS-measured temperature profiles indicate a deep stable surface layer extending up to 200 m and a weakly stable upper layer (Sec. 3.1.2). Both models overestimate the near-surface temperature (by ~2.1 K in AA25 and ~4.6 K in AS05) and underestimate the thickness of the surface layer inversion. Hereby, AS05 yields higher near-surface temperatures, only a very shallow surface-based inversion and a weakly stratified upper layer.

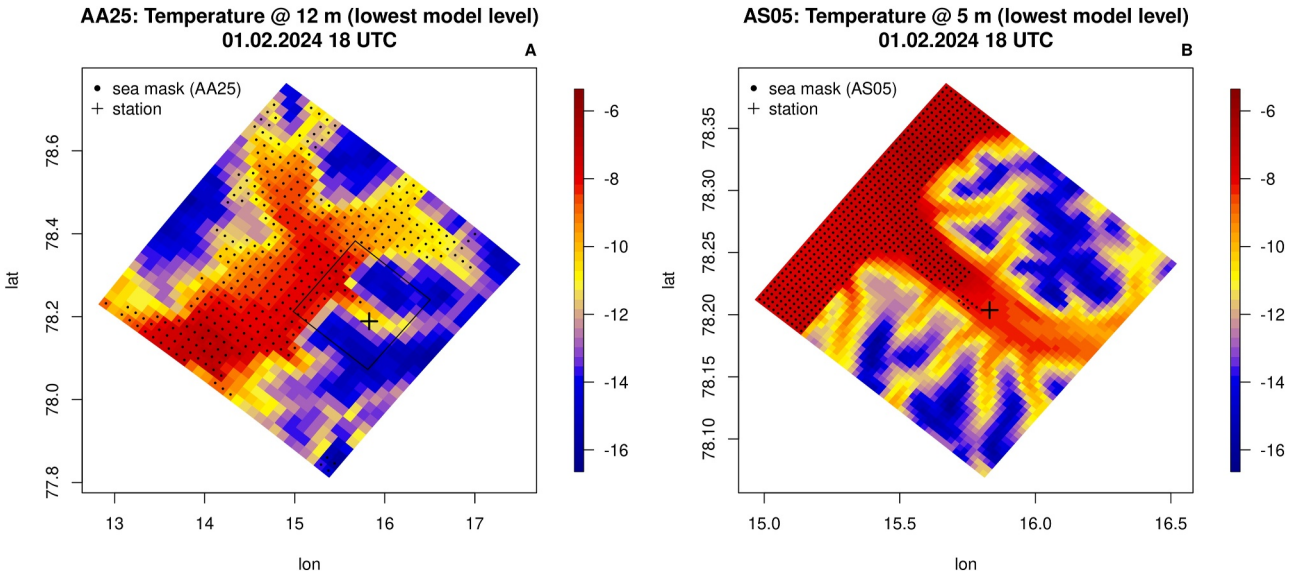

Figure 8. Same as Figure 6 on 01.02.2024 18 UTC.

The wind profile measured by the tethered sonde during the ascent shows a LLJ at a height of 45 m, above which the wind speed decreases, reaching a minimum value at the top of the surface layer inversion. AA25 partly captures the shape of the wind profile in the lowest 400 m, while AS05 overestimates the wind speeds across the profile. Both models see inflow conditions in the entire boundary layer column that are contrary to the ground-based observations (Sec. 3.1.2). As AS05 models higher wind speeds, the horizontal temperature advection of the warmer air from the fjord toward the valley is stronger, resulting in enhanced mixing, that prevents cold pool formation and thus leads to the strong warm bias in the near-surface temperature.

The AS05 model shows a high temporal variability during this night which is indicated by the dotted lines in Figure 9 representing the profiles at 2 UTC. The wind speed decreases over time across the entire boundary layer, and at the same time, the wind direction changes in the lowermost model levels from inflow via southerly to

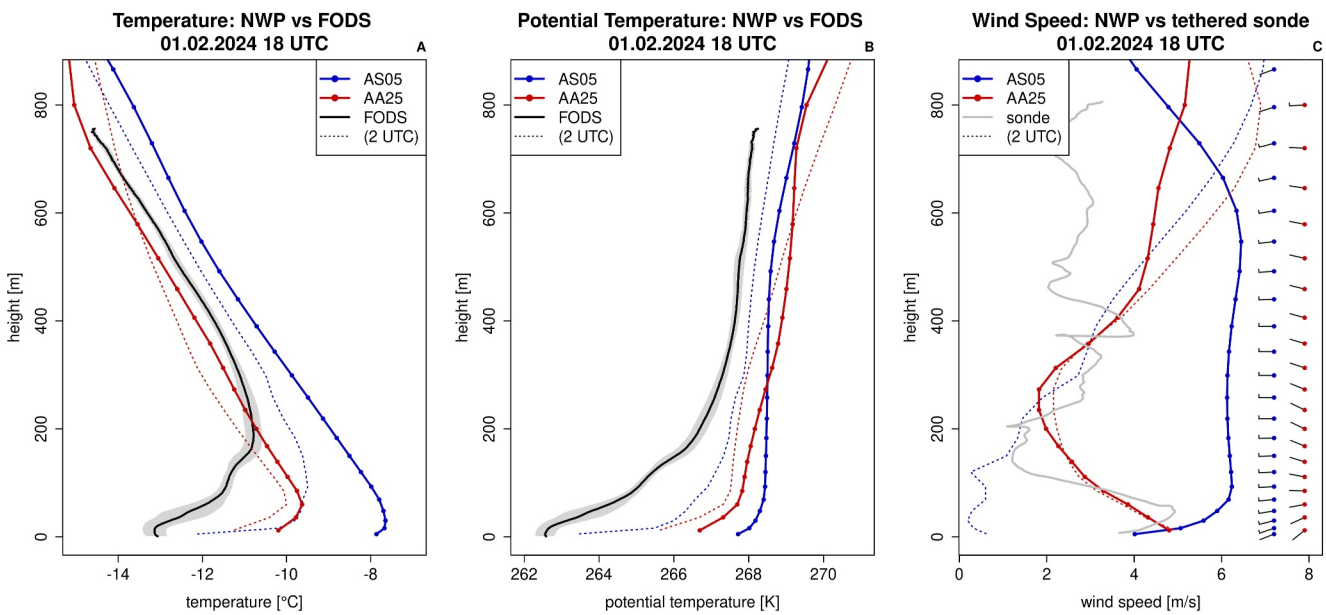

Figure 9. Same as Figure 7 on 01.02.2014 18 UTC. In addition, the dotted lines represent the respective (potential) temperature and wind speed profiles from AS05 and AA25 on 02.02.2024 2 UTC.

outflow, and a strong surface-based inversion develops (minimum temperature of −12.2°C at the lowest model level) accompanied by cold pool formation in Adventdalen. In contrast, AA25 models inflow conditions throughout the night and the inversion intensifies only slightly, reaching a minimum temperature of −11.3°C (at the lowest model level at 2 UTC), accompanied by a deepening of the boundary layer.

Combining the comparisons of both flights demonstrates that AS05 is able to represent temporal and spatial variations in the SBL in this fjord-valley system. Conversely, the coarser AA25 model shows less variability, and cannot fully capture all SBL features, especially the cold pool formation (flight 1). However, AS05 does not necessarily yield better model performance when compared to observations. By better capturing the variability, AS05 is more prone to errors emerging from, for example, incorrect meso-scale wind speed and direction that can lead to strong deviations from the observations (flight 2). AA25 is more 'resilient' to such errors and outperforms AS05 in these cases.

4. Discussion

4.1. Stable Boundary Layer Profiling With Fiber-Optic Distributed Sensing

The high resolution of the temperature measurements from FODS allows for detecting spatially fine and short-lived structures. The profiles from flight 1 represent a 'classical' stable case, where a strong surface-based inversion develops during valley outflow conditions. This is driven by radiative cooling, resulting in a consistently negative sensible heat flux. The surface-based inversion is shallow with depths less than 100 m commonly found in the European Arctic (Zhang et al., 2011). However, the inversion strength reaches up to 0.2 Km^{-1} exceeding climatological averages derived from radiosonde data (Noad & Bonnaventure, 2022; Zhang et al., 2011), but within the observed range in previous FODS studies (Fritz et al., 2021). The fact that FODS measures stronger gradients could be related to the higher spatio-temporal resolution and the continuity of the observations such that they are in an Eulerian and not in a Lagrangian frame. The FODS measurements further reveal that the surface-based inversion has a vibrant dynamic with variable altitude and regularly detaches from the surfaces. Such inversions that detach from the ground are commonly referred to as lifted inversions and occur when the near-surface temperature increases (Emeis et al., 2004). Additionally, elevated valley inversions are present, which only form during weak synoptic forcing (i.e. in flight 1, not in flight 2) and are accompanied by a thin layer of unstable stratification below and high temperature variance indicating locally enhanced mixing between the air in the valley and the one aloft (Wagner et al., 2014).

Although flight 2 is characterized by stable stratification as well, it shows inherently different dynamics: The surface-based inversion strength is weaker, but has a larger vertical extent (up to 200 m). The sensible heat flux becomes even positive when the inversion detaches from the ground, which is remarkable since the surface layer is on average still stably stratified. A warm front accompanied by a wind direction shift from valley outflow to inflow can be identified in the FODS measurements, which indicates that in this case warm air advection acts as an additional mechanism for the formation of stable stratification (e.g., Atlaskin & Vihma, 2012). The fluxes respond immediately when the warmer air mass touches the ground, and the sensible heat flux drops from 0 to −30 Wm^{-2} within minutes, while TKE and temperature variance increase, indicating strong non-stationarity.

The FODS measurements further show that the strong stability in the inversions and fronts goes along with high temperature variance, which are related to buoyancy fluctuations. This is in agreement with theoretical studies, which show that buoyancy fluctuations can even generate non-gradient heat transport (Zilitinkevich et al., 2007, 2008).

4.2. Validating HARMONIE-AROME With Fiber-Optic Distributed Sensing and Tethered Sonde Observations

The temporally and spatially continuous FODS temperature measurements allow for adapting the averaging intervals precisely to model outputs (without assuming Taylor's hypothesis) and are therefore especially suitable for model verification studies.

During the weak synoptic forcing of flight 1, characteristic SBL features develop, which are known to be challenging to reproduce for NWP models (Sandu et al., 2013). During flight 1, the coarser operational model AA25 does not reproduce the formation of cold pool and LLJ, resulting in a warm bias of ∼8 K in near-surface temperatures. In contrast, the higher-resolution model AS05 is able to capture the formation of a cold pool and

LLJ leading to a good agreement of vertical temperature and wind speed profiles with FODS and tethered sonde observations. This suggests that both a detailed representation of the orography due to higher horizontal resolution and a higher vertical resolution are beneficial for resolving various SBL features. This finding is in general agreement with Valkonen et al. (2020), who find a better performance of AS05 compared to AA25 during cold pool formation, although in their case AS05 still shows a warm bias resulting in an underestimation of the cold pool intensity. The AS05 model used here featured the updated multi-layer snow scheme and resulted in better model-observation match, which could indicate the role of a better representation of ground heat flux to reproduce near-surface temperatures consistent with Arduini et al. (2019); J. J. Day et al. (2020). Furthermore, the reduced height of the lowest model level in AS05 seems to be necessary to represent the distinct near-surface wind maximum of a LLJ, which was already suspected for the representation of surface-based temperature inversions by Hanna and Yang (2001).

During flight 2, a strong change in background flow caused highly variable flow conditions. Both models incorrectly represent the flow direction in the valley, showing inflow instead of outflow. In addition, they underestimate the surface inversion thickness, leading to a warm bias. This bias is more pronounced in AS05 compared to AA25. AS05 captures the valley channeling more accurately, albeit in the wrong direction, leading to higher wind speeds and subsequently enhanced advection of warm air from the fjord. The result is a less stable SBL, which allows for more efficient diffusive mixing, which is detrimental to the representation of inversions (Wagner et al., 2014). However, AS05 shows a high temporal variability during this night in contrast to AA25. Its modeled wind direction changes capture the observed valley outflow with the deepening surface layer inversion in the later part of the night.

Overall, higher resolution and accurate topography substantially improve the vertical representation of the SBL structure during weak synoptic forcing when land-atmosphere interactions exert a strong forcing. Thereby, the ability to correctly model the near-surface temperatures depends strongly on the correct representation of the surface-based temperature inversion profile (Atlaskin & Vihma, 2012). However, during varying flow conditions and synoptic forcing, high-resolution models, especially with strong numerical diffusion, are very sensitive to the representation of the flow, which may lead to worse performance compared to coarser models in case when the background flow is misrepresented. This finding also suggests that model evaluation studies should explicitly include the temporal evolution in addition to the spatial variability (Kähnert et al., 2022).

Our results further confirm the findings of Wagner et al. (2014), who study the effect of different horizontal resolutions on the boundary layer representation in an idealized valley, for a real-world valley system. Wagner et al. (2014) find that unresolved topography due to smoothed valley geometry in coarser resolutions deprives the model of the ability to correctly represent valley circulations and inversions–and this topography effect also dominates the influence of non-resolved turbulence (parameterization). They further find that the ratio between nominal model resolution Δx and valley width L determines the model's ability to represent the flow and suggest a rough threshold of $\Delta x/L \leq 0.1$. In our case for the approximately 4 km wide Adventdalen valley, $\Delta x/L = 0.125$ for AS05 and $\Delta x/L = 0.625$ for AA25, such that AS05 may feature just enough grid points to cover the entire valley geometry in contrast to AA25. At the same time AS05 does not represent the geometry of the smaller side valleys with a sufficient level of detail, which is probably the reason why they do not feature cold pool development during the first flight. This suggests that $\Delta x/L$ could be a crucial scaling parameter for the further development of parameterizations of SBLs in valley systems, which may benefit from utilizing non-local topographical information.

5. Conclusions

We collected temperature profiles of the Arctic SBL under different flow conditions with airborne FODS up to ~900 m combined with ground-based EC measurements during the polar night in Adventdalen, Svalbard. The temporally and spatially highly resolved FODS temperature measurements allow for capturing inherent features of the SBL, such as surface-based and elevated valley inversions, and their spatio-temporal variability and thus provide a valuable context for the interpretation of EC measurements at the surface.

The comparison of the measurements to the HARMONIE-AROME model showed that under weak synoptic forcing, the higher-resolution model (AS05) outperforms the coarser model (AA25), which has a warm bias of about 8 K in the near-surface temperature. In agreement with the observations, AS05 models the formation of a cold pool in Adventdalen accompanied by a low-level jet aloft, whereas AA25 does not represent these typical

SBL features. This points to the crucial role of the ratio between nominal model resolution and valley width $\Delta x/L$ to represent these distinct SBL features. During changing background flow conditions, AS05 is more sensitive to a misrepresented wind direction and speed, but at the same time can respond more rapidly to their changes.

Data Availability Statement

The field data are available under https://doi.org/10.17605/OSF.IO/K28DE (Mack et al., 2024). The model data provided by the Norwegian Meteorological Institute (MET Norway) can be found in the thredds archive under https://thredds.met.no/thredds/catalog/aromearcticarchive/2024/catalog.html (for AA25) and https://thredds.met.no/thredds/catalog/finis/UNIS-2024/catalog.html (for AS05).

Acknowledgments
The University Centre in Svalbard (UNIS) is acknowledged for logistical and financial support of the fieldwork. We would like to thank Bolli Palmason for preparing the updated physiography data used in the experiment AS05. Geospatial support for this work was provided by the Polar Geospatial Center under NSF-OPP awards 1043681, 1559691, and 2129685. ArcticDEM data were provided by the Polar Geospatial Center under NSF-OPP awards 1043681, 1559691, 1542736, 1810976, and 2129685. The work was supported by the Research Council of Norway (project #301552), and the European Research Council (project #101116083, and grant agreement #724629 - DarkMix).

References

Arduini, G., Balsamo, G., Dutra, E., Day, J. J., Sandu, I., Bousetta, S., & Haiden, T. (2019). Impact of a multi-layer snow scheme on near-surface weather forecasts. *Journal of Advances in Modeling Earth Systems*, *11*(12), 4687–4710. https://doi.org/10.1029/2019MS001725

Atlaskin, E., & Vihma, R. (2012). Evaluation of NWP results for wintertime nocturnal boundary-layer temperatures over Europe and Finland. *Quarterly Journal of the Royal Meteorological Society*, *138*(667), 1440–1451. https://doi.org/10.1002/qj.1885

Banta, R. M. (2008). Stable-boundary-layer regimes from the perspective of the low-level jet. *Acta Geophysica*, *56*(1), 58–87. https://doi.org/10.2478/s11600-007-0049-8

Beljaars, A., Balsamo, G., Betts, A., Dutra, E., Ghelli, A., Köhler, M., et al. (2011). The stable boundary layer in the ECMWF model. *ECMWF GABLS Workshop on Diurnal cycles and the stable boundary layer*.

Beljaars, A., & Viterbo, P. (1998). The role of the boundary layer in a numerical weather prediction model. *Roy. Netherlands Acad. of Arts and Sci.*, 287–304.

Bengtsson, L., Andrae, U., Aspelien, T., Batrak, Y., Calvo, J., de Rooy, W., et al. (2017). The HARMONIE–AROME model configuration in the ALADIN–HIRLAM NWP system. *Monthly Weather Review*, *145*(5), 1919–1935. https://doi.org/10.1175/MWR-D-16-0417.1

Bintanja, R., Graversen, R. G., & Hazeleger, W. (2011). Arctic winter warming amplified by the thermal inversion and consequent low infrared cooling to space. *Nature Geoscience*, *4*(11), 758–761. https://doi.org/10.1038/NGEO1285

Cuxart, J., Holtslag, A. A. M., Beare, R. J., Bazile, E., Beljaars, A., Cheng, A., et al. (2006). Single-column model intercomparison for a stably stratified atmospheric boundary layer. *Boundary-Layer Meteorology*, *118*(2), 273–303. https://doi.org/10.1007/s10546-005-3780-1

Danielson, J. J., & Gesch, D. B. (2011). Global multi-resolution terrain elevation data 2010 (GMTED2010). Report. *Technical Reports Series*. https://doi.org/10.3133/ofr20111073

Day, J., Svensson, G., Casati, B., Uttal, T., Khalsa, S.-J., Bazile, E., et al. (2024). The YOPP site model intercomparison project (YOPPsiteMIP) phase 1: Project overview and arctic winter forecast evaluation. *Geoscientific Model Development*, *17*(14), 5511–5543. https://doi.org/10.5194/gmd-17-5511-2024

Day, J. J., Arduini, G., Sandu, I., Magnusson, L., Beljaars, A., Balsamo, G., et al. (2020). Measuring the impact of a new snow model using surface energy budget process relationships. *Journal of Advances in Modeling Earth Systems*, *12*, e2020MS002144. https://doi.org/10.1029/2020MS002144

Decharme, B., Boone, A., Delire, C., & Noilhan, J. (2011). Local evaluation of the interaction between soil biosphere atmosphere soil multilayer diffusion scheme using four pedotransfer functions. *JGR Atmospheres*, *116*(D20), D20126. https://doi.org/10.1029/2011JD016002

Derbyshire, S. (1999). Boundary-layer decoupling over cold surfaces as a physical boundary-instability. *Boundary-Layer Meteorology*, *90*(2), 297–325. https://doi.org/10.1023/a:1001710014316

des Tombe, B., Schilperoort, B., & Bakker, M. (2020). Estimation of temperature and associated uncertainty from fiber-optic Raman-spectrum distributed temperature sensing. *Sensors*, *20*(8), 2235. https://doi.org/10.3390/s20082235

Emeis, S., Münkel, C., Vogt, S., Mler, W. J., & Schäfer, K. (2004). Atmospheric boundary-layer structure from simultaneous SODAR, RASS, and ceilometer measurements. *Atmospheric Environment*, *38*(2), 273–286. https://doi.org/10.1016/j.atmosenv.2003.09.054

Esau, I., Tolstykh, M., Fadeev, R., Shashkin, V., Makhnorylova, S., Miles, V., & Melnikov, V. (2018). Systematic errors in northern Eurasian short-term weather forecasts induced by atmospheric boundary layer thickness. *Environmental Research Letters*, *13*(12), 125009. https://doi.org/10.1088/1748-9326/aaecfb

Foken, T. (2017). *Micrometeorology*. Springer.

Fritz, A. M., Lapo, K., Freundorfer, A., Linhardt, T., & Thomas, C. K. (2021). Revealing the morning transition in the mountain boundary layer using fiber–optic distributed temperature sensing. *Geophysical Research Letters*, *48*(9). https://doi.org/10.1029/2020GL092238

Hanna, S. R., & Yang, R. (2001). Evaluations of mesoscale models' simulations of near-surface winds, temperature gradients, and mixing depths. *Journal of Applied Meteorology*, *40*(6), 1095–1104. https://doi.org/10.1175/1520-0450(2001)040<1095:eommso>2.0.co;2

Kähnert, M., Sodemann, H., Remes, T. M., Fortelius, C., Bazile, E., & Esau, I. (2022). Spatial variability of nocturnal stability regimes in an operational weather prediction model. *Boundary-Layer Meteorology*, *186*(2), 373–397. https://doi.org/10.1007/s10546-022-00762-1

Køltzow, M., Casati, B., Bazile, E., Haiden, T., & Valkonen, T. (2019). An NWP model intercomparison of surface weather parameters in the European arctic during the year of polar prediction special observing period northern hemisphere 1. *Weather and Forecasting*, *34*(4), 959–983. https://doi.org/10.1175/WAF-D-19-0003.1

Lapo, K., & Freundorfer, A. (2020). klapo/pyfocs v0.5. Retrieved from https://doi.org/10.5281/zenodo.4292491

Lehner, M., & Rotach, M. W. (2018). Current challenges in understanding and predicting transport and exchange in the atmosphere over mountainous terrain. *MDPI Atmosphere*, *9*(276), 276. https://doi.org/10.3390/atmos9070276

Lenderink, G., & Holtslag, A. A. M. (2004). An updated length-scale formulation for turbulent mixing in clear and cloudy boundary layers. *Quarterly Journal of the Royal Meteorological Society*, *130*(604), 3405–3427. https://doi.org/10.1256/qj.03.117

Li, D., & Bou-Zeid, E. (2011). Coherent structures and the dissimilarity of turbulent transport of momentum and scalars in the unstable atmospheric surface layer. *Boundary-Layer Meteorology*, *140*(2), 243–262. https://doi.org/10.1007/s10546-011-9613-5

Louis, J. F. (1979). A parameteric model of vertical eddy fluxes in the atmosphere. *Boundary-Layer Meteorology*, *17*(2), 187–202. https://doi.org/10.1007/bf00117978

Mack, L., Kähnert, M., Rauschenbach, Q., Hasenburg, F. H., Huss, J., Jonassen, M. O., et al. (2024). Airborne fiber-optic distributed sensing in Adventdalen, Svalbard [dataset]. *OSF*. Retrieved from https://doi.org/10.17605/OSF.IO/K28DE

Mahrt, L. (2014). Stably stratified atmospheric boundary layers. *Annual Review of Fluid Mechanics*, *46*(1), 23–45. https://doi.org/10.1146/annurev-fluid-010313-141354

Masson, V., Le Moigne, P., Martin, E., Faroux, S., Alias, A., Alkama, R., et al. (2013). The SURFEXv7.2 land and ocean surface platform for coupled or offline simulation of earth surface variables and fluxes. *Geoscientific Model Development*, *6*(4), 929–960. https://doi.org/10.5194/gmd-6-929-2013

Mayer, S., Jonassen, M. O., Sandvik, A., & Reuder, J. (2012). Profiling the arctic stable boundary layer in advent valley, svalbard: Measurements and simulations. *Boundary-Layer Meteorology*, *143*(3), 507–526. https://doi.org/10.1007/s10546-012-9709-6

Mazzola, M., Tampieri, F., Viola, A., Lanconelli, C., & Choi, T. (2016). Stable boundary layer vertical scales in the Arctic: Observations and analyses at Ny-Ålesund, Svalbard. *Quarterly Journal of the Royal Meteorological Society*, *142*(696), 1250–1258. https://doi.org/10.1002/qj.2727

Müller, M., Batrak, Y., Kristiansen, J., Køltzow, M. A. Ø., Noer, G., & Korosov, A. (2017a). Characteristics of a convective-scale weather forecasting system for the European arctic. *Monthly Weather Review*, *145*(12), 4771–4787. https://doi.org/10.1175/MWR-D-17-0194.1

Müller, M., Homleid, M., Ivarsson, K.-I., Køltzow, M. A., Lindskog, M., Midtbø, K. H., et al. (2017b). AROME-MetCoOp: A nordic convective-scale operational weather prediction model. *Weather and Forecasting*, *32*(2), 609–627. https://doi.org/10.1175/WAF-D-16-0099.1

Noad, N. C., & Bonnaventure, P. P. (2022). Surface temperature inversion characteristics in dissimilar valleys, Yukon Canada. *Arctic Science*, *8*, 1320–1339. https://doi.org/10.1139/AS-2021-0048

Pfister, L., Lapo, K., Mahrt, L., & Thomas, C. K. (2021a). Thermal submeso motions in the nocturnal stable boundary layer. Part 2: Generating mechanisms and implications. *Boundary-Layer Meteorology*, *180*(2), 203–224. https://doi.org/10.1007/s10546-021-00619-z

Pfister, L., Lapo, K., Mahrt, L., & Thomas, C. K. (2021b). Thermal submesoscale motions in the nocturnal stable boundary layer. Part 1: Detection and mean statistics. *Boundary-Layer Meteorology*, *180*(2), 187–202. https://doi.org/10.1007/s10546-021-00618-0

Pietroni, I., Argentini, S., & Petenko, I. (2014). One year of surface-based temperature inversions at dome C, Antarctica. *Boundary-Layer Meteorology*, *150*(1), 131–151. https://doi.org/10.1007/s10546-013-9861-7

Pirk, N., Sievers, J., Mertes, J., Parmentier, F.-J. W., Mastepanov, M., & Christensen, T. R. (2017). Spatial variability of CO_2 uptake in polygonal tundra: Assessing low-frequency disturbances in eddy covariance flux estimates. *Biogeosciences*, *14*(12), 3157–3169. https://doi.org/10.5194/bg-14-3157-2017

Porter, C., Morin, P., Howat, I., Noh, M.-J., Bates, B., Peterman, K., et al. (2018). ArcticDEM, version 3. *Harvard Dataverse*. Retrieved from https://doi.org/10.7910/DVN/OHHUKH

Sandu, I., Beljaars, A., Bechthold, P., et al. (2013). Why is it so difficult to represent stably stratified conditions in numerical weather prediction (NWP) models? *Journal of Advances in Modeling Earth Systems*, *5*, 117–133. https://doi.org/10.1002/jame.20013,2013

Savijärvi, H. (2014). High-resolution simulations of the night-time stable boundary layer over snow. *Quarterly Journal of the Royal Meteorological Society*, *140*(680), 1121–1128. https://doi.org/10.1002/qj.2187

Selker, J., van de Giesen, N., Westhoff, M., Luxemburg, W., & Parlange, M. B. (2006). Fiber optics opens window on stream dynamics. *Geophysical Research Letters*, *33*(L24401). https://doi.org/10.1029/2006GL027979

Serafin, S., Adler, B., Cuxart, J., De Wekker, S., Gohm, A., Grisogono, B., et al. (2018). Exchange processes in the atmospheric boundary layer over mountainous terrain. *MDPI Atmosphere*, *9*(102), 102. https://doi.org/10.3390/atmos9030102

Sigmund, A., Pfister, L., Sayde, C., & Thomas, C. K. (2017). Quantitative analysis of the radiation error for aerial coiled-fiber-optic distributed temperature sensing deployments using reinforcing fabric as support structure. *Atmospheric Measurement Techniques*, *10*(6), 2149–2162. https://doi.org/10.5194/amt-10-2149-2017

Smith, S. L., & Bonnaventure, P. P. (2017). Quantifying surface temperature inversions and their impact on the ground thermal regime at a high arctic site. *Arctic, Antarctic, and Alpine Research*, *49*(1), 173–185. https://doi.org/10.1657/AAAR0016-039

Steeneveld, G.-J., Nappo, C. J., & Holtslag, A. A. M. (2009). Estimation of orographically induced wave drag in the stable boundary layer during the CASES-99 experimental campaign. *Acta Geophysica*, *57*(4), 857–881. https://doi.org/10.2478/s11600-009-0028-3

Taylor, P. C., Boeke, R. C., Boisvert, L. N., Feldl, N., Henry, M., Huang, Y., et al. (2022). Process drivers, inter-model spread, and the path forward: A review of amplified arctic warming. *Frontiers of Earth Science*, *9*(758361). https://doi.org/10.3389/feart.2021.758361

Thomas, C. K., Kennedy, A. M., Selker, J. S., Moretti, A., Schroth, M. H., Smoot, A. R., et al. (2012). High-resolution fibre-optic temperature sensing: A new tool to study the two-dimensional structure of atmospheric surface-layer flow. *Boundary-Layer Meteorology*, *142*(2), 177–192. https://doi.org/10.1007/s10546-011-9672-7

Tjernstroem, M., Svensson, G., Magnusson, L., Brooks, I. M., Prytherch, J., Vüllers, J., & Young, G. (2021). Central arctic weather forecasting: Confronting the ECMWF IFS with observations from the arctic ocean 2018 expedition. *Quarterly Journal of the Royal Meteorological Society*, *147*(735), 1278–1299. https://doi.org/10.1002/qj.3971

Valkonen, T., Stoll, P., Batrak, Y., Køltzow, M., Schneider, T. M., Stigter, E. E., et al. (2020). Evaluation of a sub-kilometre NWP system in an Arctic fjord-valley system in winter. *Tellus A*, *72*(1838181), 1838181. https://doi.org/10.1080/16000870.2020.1838181

Viana, S., Yagüe, C., & Maqueda, G. (2012). Vertical structure of the stable boundary layer detected by RASS-SODAR and in-situ measurements in SABLES 2006 field campaign. *Acta Geophysica*, *60*(5), 1261–1286. https://doi.org/10.2478/s11600-011-0072-7

Wagner, J. S., Gohm, A., & Rotach, M. W. (2014). The impact of horizontal model grid resolution on the boundary layer structure over an idealized valley. *Monthly Weather Review*, *142*(9), 3446–3465. https://doi.org/10.1175/MWR-D-14-00002.1

Wyngaard, J. C., & Coté, O. R. (1971). The budgets of turbulent kinetic energy and temperature variance in the atmospheric surface layer. *Journal of the Atmospheric Sciences*, *28*(2), 190–201. https://doi.org/10.1175/1520-0469(1971)028<0190:tbotke>2.0.co;2

Zeeman, M. J., Selker, J. S., & Thomas, C. K. (2015). Near-surface motion in the nocturnal, stable boundary layer observed with fibre-optic distributed temperature sensing. *Boundary-Layer Meteorology*, *154*(2), 189–205. https://doi.org/10.1007/s10546-014-9972-9

Zeller, M.-L., Huss, J.-M., Pfister, L., Lapo, K. E., Littmann, D., Schneider, J., et al. (2021). The NY-Ålesund TurbulencE Fiber Optic eXperiment (NYTEFOX): Investigating the Arctic boundary layer, Svalbard. *Earth System Science Data*, *13*(7), 3439–3452. https://doi.org/10.5194/essd-13-3439-2021

Zhang, Y., Seidel, D. J., Golaz, J.-C., Deser, C., & Tomas, R. A. (2011). Climatological characteristics of Arctic and Antarctic surface-based inversions. *Journal of Climate*, *24*(19), 5168–5186. https://doi.org/10.1175/2011JCLI4004.1

Zilitinkevich, S. S., Elperin, T., Kleeorin, N., & Rogachevskii, I. (2007). Energy- and flux-budget (EFB) turbulence closure model for stably stratified flows. Part I: Steady-state, homogeneous regimes. *Boundary-Layer Meteorology*, *125*(2), 167–191. https://doi.org/10.1007/s10546-007-9189-2

Zilitinkevich, S. S., Elperin, T., Kleeorin, N., Rogachevskii, I., Esau, I., Mauritsen, T., & Miles, M. W. (2008). Turbulence energetics in stably stratified geophysical flows: Strong and weak mixing regimes. *Quarterly Journal of the Royal Meteorological Society*, *134*(633), 793–799. https://doi.org/10.1002/qj.264